Copyright WILEY-VCH Verlag GmbH & Co. KGaA, 69469 Weinheim, Germany, 2020.

ADVANCED
OPTICAL
MATERIALS

Supporting Information

for *Adv. Optical Mater.,* DOI: 10.1002/adom.202000720

Efficient Er/O-Doped Silicon Light-Emitting Diodes at Communication Wavelength by Deep Cooling

Huimin Wen, Jiajing He, Jin Hong, Shenbao Jin, Zhenming Xu, Hong Zhu, Jingquan Liu, Gang Sha, Fangyu Yue, and Yaping Dan**

Copyright WILEY-VCH Verlag GmbH & Co. KGaA, 69469 Weinheim, Germany, 2020.

Supporting Information

Efficient Er/O Doped Silicon Light-Emitting Diodes at Communication Wavelength by Deep Cooling

Huimin Wen, Jiajing He, Jin Hong, Shenbao Jin, Zhenming Xu, Hong Zhu, Jingquan Liu, Gang Sha, Fangyu Yue, and Yaping Dan**

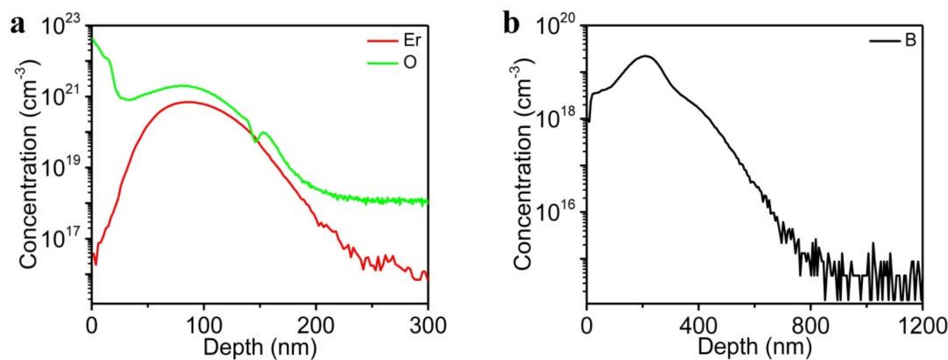

Figure S1. SIMS characterization of Er/O-doped Si samples and devices. a) Erbium (red line) and Oxygen (green line) ion distribution profiles of the DC-processed Er/O-Si sample (to 300 nm below surface) by SIMS measurements. b) Boron ion distribution profile of Er/O-Si LED devices by SIMS measurements.

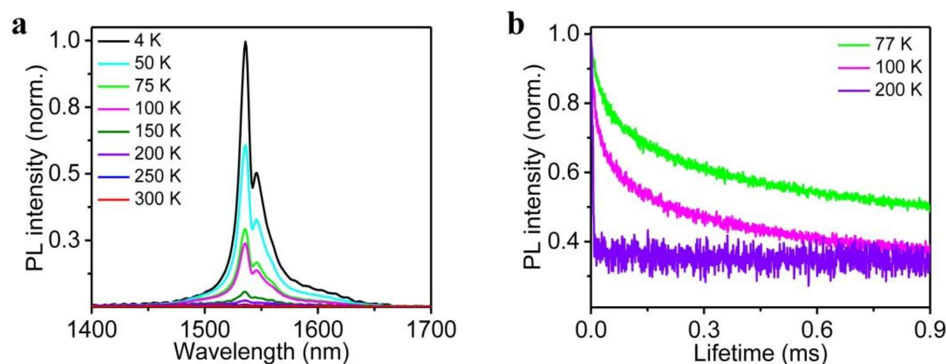

Figure S2. Temperature-dependent PL spectra of Er/O-Si samples. a) Temperature-dependent PL spectra of the RTA-processed sample, which was measured as a comparison with the results in Figure 1a. b) Lifetime curves at 1536 nm as a function of temperature for the DC-processed sample. As the temperature increases, the slow component in RTA-processed samples gradually disappears, especially at room temperature.

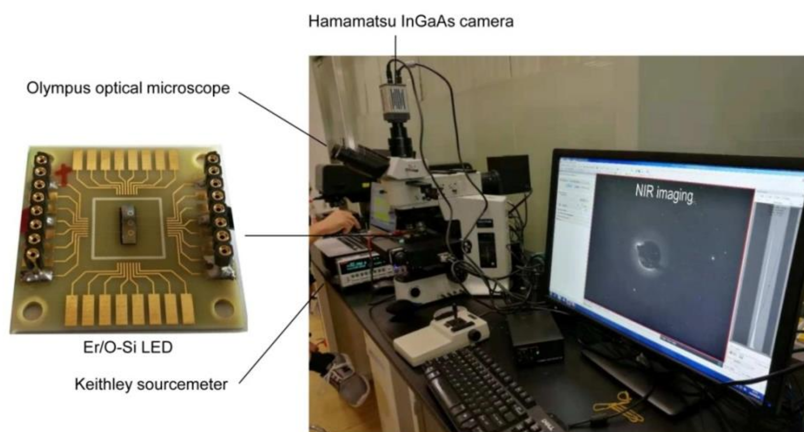

Figure S3. Room-temperature NIR imaging setup. An NIR Olympus optical microscope equipped with a Hamamatsu InGaAs camera (0.90 - 1.70 μm) was used to image the electrically-pumped emission (Keithley sourcemeter) from LED devices that is treated with the DC process. The optical image of PCB-integrated Er/O-Si LED devices was also displayed.

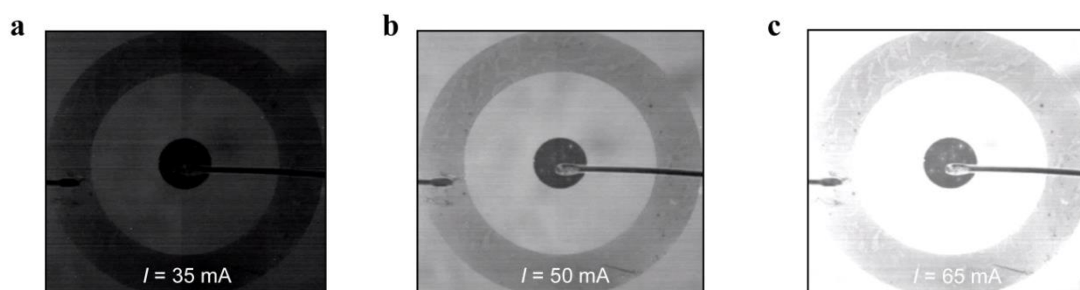

Figure S4. Optoelectronic properties of Er/O-Si LED devices treated by the deep cooling process. NIR microscopic images of the device emission under electrical pumping with a) 35 mA, b) 50 mA, and c) 65 mA injection current.

Supplementary Video. This short video shows the lightening-up process of the DC-processed Er/O-Si LED device at room temperature. The detailed NIR imaging setup, including optical microscope, InGaAs camera, and semiconductor parameter system etc. is shown in Figure S3. The video shows that the recorded EL brightness of Er/O-Si LED devices increased significantly until the instant radiation overexposure occurred at room temperature, as the injected current rose gradually. The inset video corresponds to the real-time *I-t* curve of Er/O-Si LED devices.

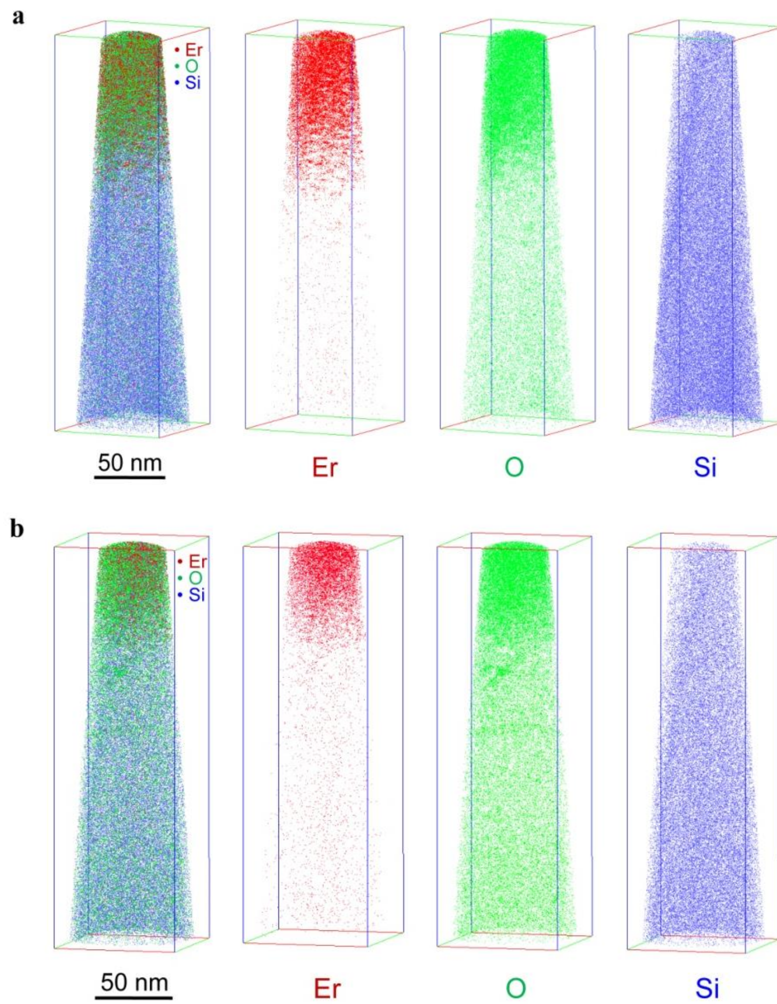

Figure S5. Three dimensional reconstruction volume of Er (red dots), O (green dots), and Si (blue dots) atoms of a) RTA- and b) DC-processed Er/O-Si samples obtained by APT techniques.

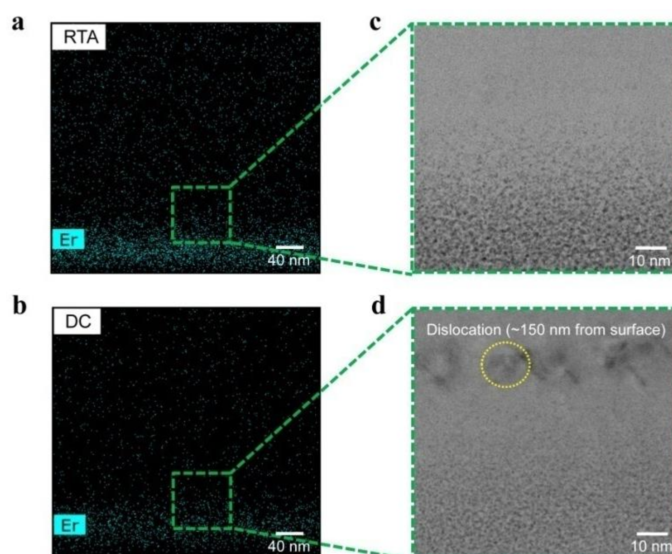

Figure S6. TEM characterization. Er EDX mapping of a) RTA- and b) DC-processed Er/O-Si samples. Cross-sectional bright field TEM image of c) RTA- and d) DC-processed Er/O-Si samples. At ~150 nm below the surface, silicon dislocations occurred after the DC treatment, enclosed by the yellow dotted circle.

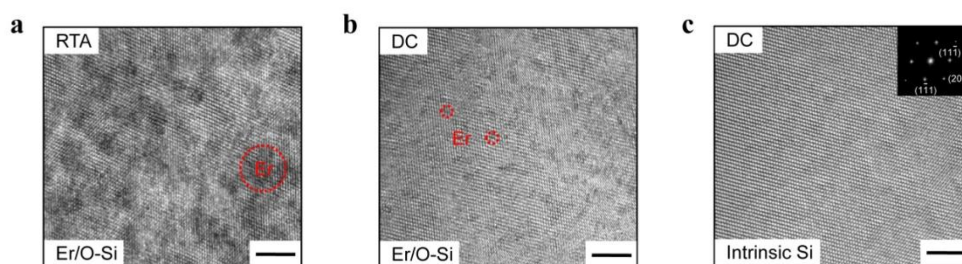

Figure S7. Microstructure characterization. High-resolution TEM image of a) RTA- and b) DC-processed Er/O-Si samples. c) High-resolution TEM image of the DC-processed intrinsic Si sample. The inset is the selected area electron diffraction of intrinsic Si samples. The Er clusters dispersing in silicon matrix are enclosed by the red dotted circle in (a) and (b). All scale bars are 5 nm in this figure.

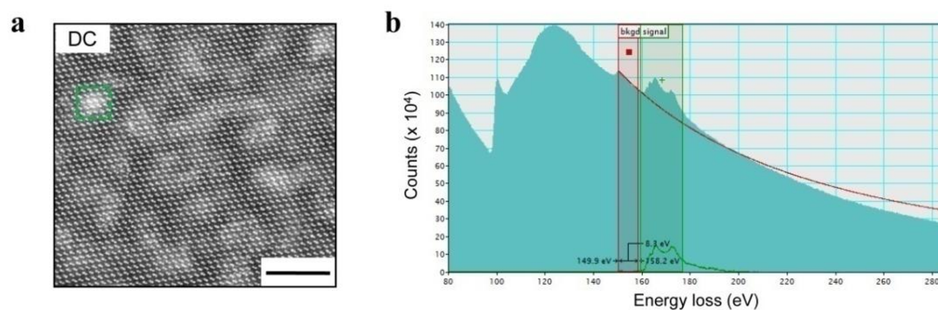

Figure S8. Composition characterization of the DC-processed Er/O-Si sample. a) Another HAADF micrograph of the DC-processed Er/O-Si sample. The scale bar is 5 nm in (a). b) EELS spectrum of the DC-processed Er/O-Si sample. The strong peaks at 168 eV and 176 eV representing the Er contribution can be displayed clearly in green curve. The green dotted square in (a) represents the area in which an EELS spectrum has been taken.

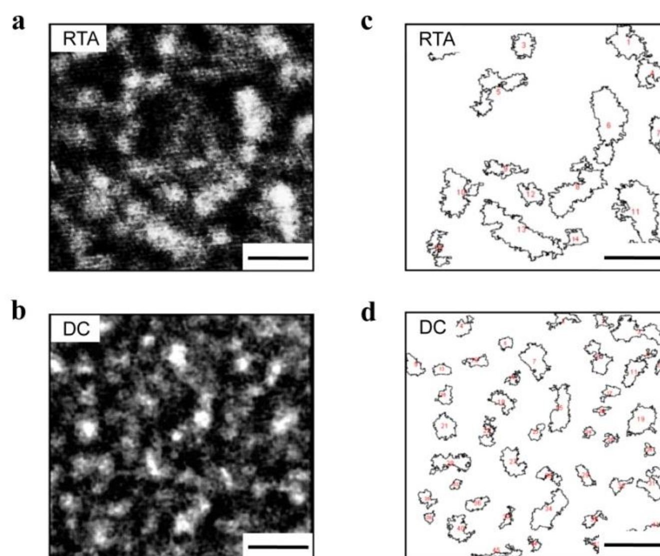

Figure S9. Microstructure analysis. HAADF micrographs of a) RTA-, and b) DC-processed Er/O-Si samples. With use of ImageJ software, the Si pattern background in (a) and (b) was subtracted for the subsequent statistical analysis of Er nanocluster size. The rough contour maps of Er nanoclusters in c) RTA- and d) DC- processed Er/O-Si samples. The recognized clusters were entitled with a sequence of red numbers (1, 2, 3......) in (c) and (d). In order to ensure the statistical accuracy, more than 100 clusters were collected. And the final histograms of Er size were shown in Figure 4c, d. All scale bars are 5 nm in this figure.

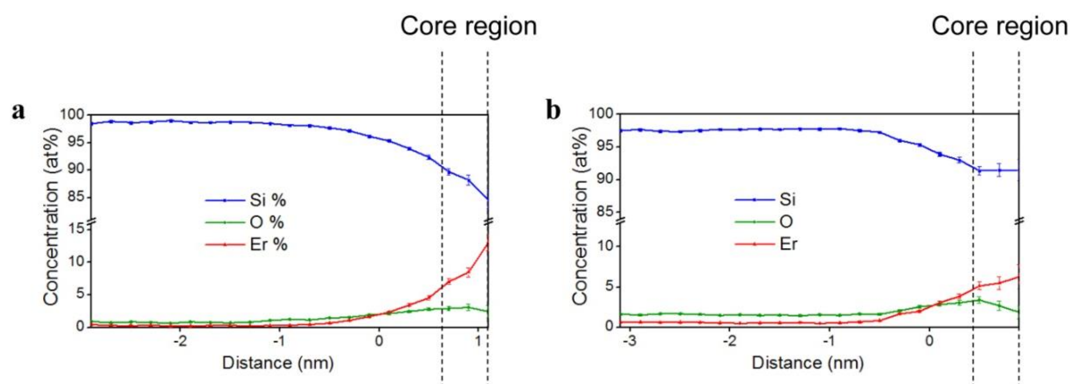

Figure S10. Composition analysis by APT technique. The core regions of the clusters in a) RTA- and b) DC-processed Er/O-Si samples were defined by 0.4 nm distance to the center. The compositions of Er nanoclusters were estimated by averaging the core concentrations of the proximity histograms produced by reconstructing 1.5% (in at%) isosurfaces in DC- and RTA-processed samples.

Table S1. Elementary composition (at. %) of Er nanoclusters by APT analysis.

Process	Si	Er	O	Er(O)	Er(Si)	Er(Si)/Er(O)
RTA	88.40	8.20	3.07	2.05	6.15	3.00
DC	91.50	5.25	3.04	2.03	3.22	1.59

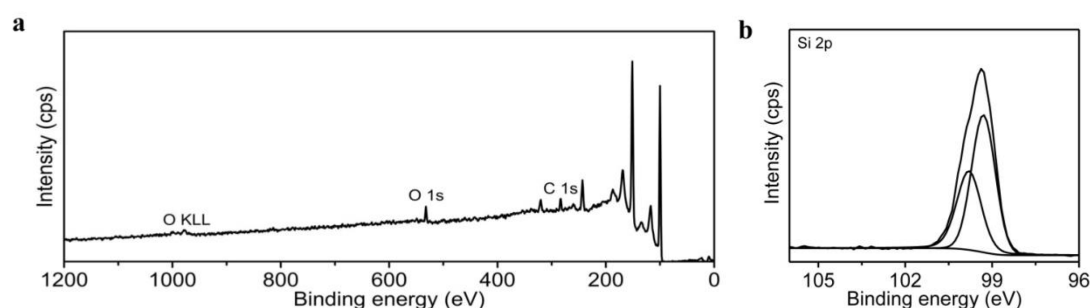

Figure S11. XPS spectra of Er/O-Si samples after RTA treatments. Survey spectra of a) the RTA-processed Er/O-Si sample. b) Narrow scan of Si 2p regions (99.3 eV and 99.8 eV) of the RTA-processed Er/O-Si sample. The XPS data in this figure was collected at ~80 nm below the Er/O-Si surface by Argon ion bombardment.

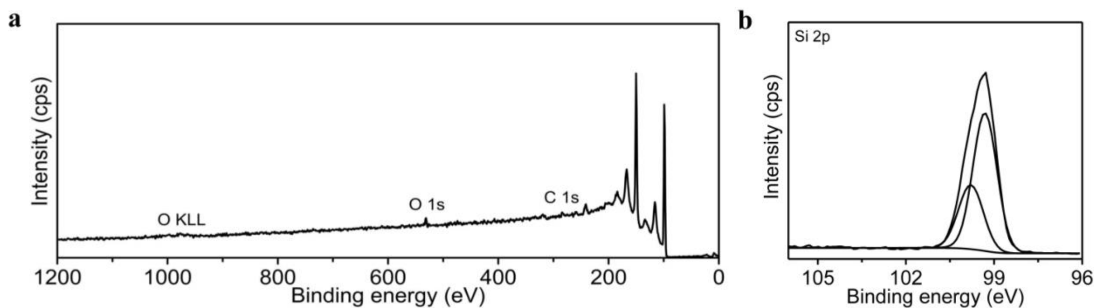

Figure S12. XPS spectra of Er/O-doped Si samples after DC treatments. Survey spectra of a) the DC-processed Er/O-Si sample. b) Narrow scan of Si 2p regions (99.3 eV and 99.8 eV) of the DC-processed Er/O-Si sample. The XPS data in this figure was collected at ~80 nm below the Er/O-Si surface by Argon ion bombardment.

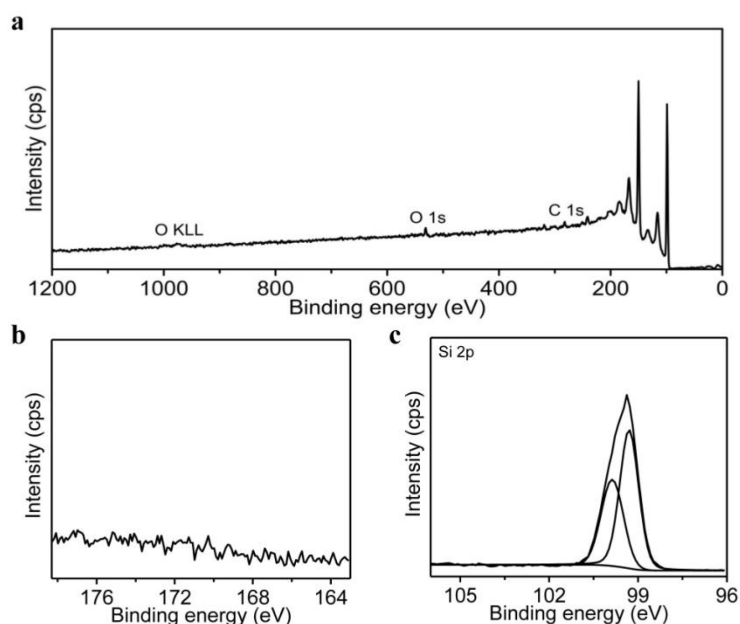

Figure S13. XPS spectra of the intrinsic Si sample for references. a) Survey spectra of the intrinsic Si sample. Narrow scan of b) Er 4d, and **c** Si 2p regions of the intrinsic Si sample. The XPS data in this figure was collected at ~80 nm below the intrinsic Si surface by Argon ion bombardment.

Supplementary Note. To prove the size effect of Er clusters in silicon, a preliminary theoretical simulation was performed for DC- and RTA-processed Er/O-doped silicon samples. Single crystalline Si and Er_2O_3 structures were adopted to simplify the calculation procedure. The interface energy, the sum of chemical and elastic energy, was evaluated within coherent and semi-coherent interface models (Figure S14a, b). The density of state (DOS) was calculated by using the projector augmented wave method in the framework of the density functional theory (DFT)[R1], as implemented in the Vienna ab-initio simulation package (VASP) software. The generalized gradient approximation (GGA) and Perdew-Burke-Ernzerhof (PBE) exchange functional was used.[R1] The plane-wave energy cutoff was set to 500 eV, and the Monkhorst-Pack method[R2] was employed for the Brillouin zone sampling of interface models. The convergence criterions of energy calculations were set to 10^{-5} eV/atom. The coherent and semi-coherent Si/Er_2O_3 interfaces were built by the (2 × 2) Si (001) and (1 × 1) Er_2O_3 (001) slabs, and the semi-coherent Si/Er_2O_3 interfaces were built by (24 × 2) Si (001) and (13 × 1) Er_2O_3 (001) slabs to study the interfacial states due to the dangling bonds since the coherent interfaces is difficult to model with periodic boundary conditions. The *k*-meshes of the coherent and semi-coherent interface calculations are 2 × 2 × 1 and 1 × 2 ×1, respectively.

The total interface energy is the sum of the chemical energy and elastic energy.[R3] Chemical energy stands for the chemistry part of total energy which stemming from breaking and forming of bonds in constructing the interface. Elastic energy is the energy originating from the lattice mismatch in the interface region. When a material A grows on the substrate B (A and B have different lattice constants), at the beginning period, the interfacial atoms of the very thin A material are fully saturated with relatively smaller chemical energies, forming the coherent A/B interface with some elastic energies. With the further growing of A material, the elastic energies will rapidly increase with the increasing thickness of the material A, and eventually the coherent A/B interface turns into semi-coherent and even non-coherent to minimize the elastic contribution to the total interface energy. In summary, the A/B interface turns from the coherent state to semi-coherent with the increase of the growth thickness of material A (Figure S15).

The elementary-projected density of state (DOS) was then obtained by DFT calculations, as shown in Figure S15c-e. It demonstrates that the potential de-excitation peak at Fermi level has been indeed eliminated, as the particle size of Er_2O_3 dopant decreases. Therefore, the developed DC process, with a result of relatively smaller size of Er/O nanoparticles and lower interface energy between Si and Er_2O_3 regions, significantly decreases the potential nonradiative possibility, and thus provides a completely new approach to high luminous efficiency for Er/O-doped Si light sources.

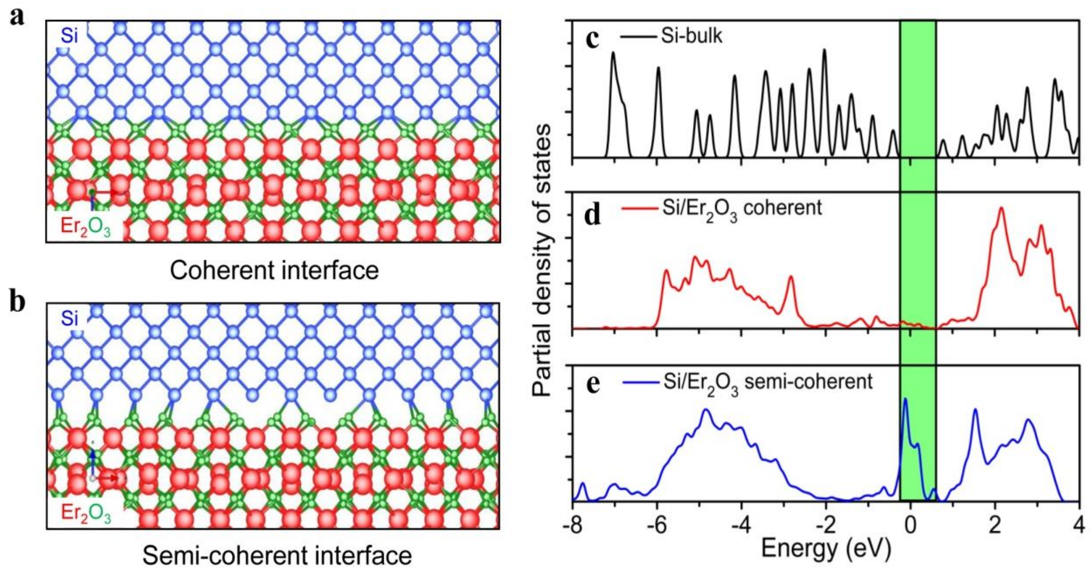

Figure S14. Theoretical simulations of nonradiative mechanism for DC- and RTA-processed Er/O-Si samples. Schematic representations of a) coherent and b) semi-coherent interface models between Si and Er_2O_3 regions. Partial DOS curves of c) Si in bulk region and Si/Er_2O_3 interfaces with d) coherent and e) semi-coherent models, respectively. The corresponding defect state density in the silicon bandgap is enclosed in the green rectangular pane.

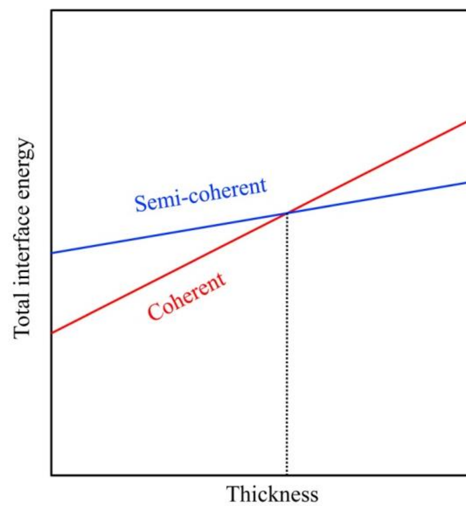

Figure S15. Thickness-dependent curves of interface energy. Coherent (red curve) and semi-coherent (blue curve) interface models were considered for DC- and RTA-processed Er/O-Si samples, respectively.

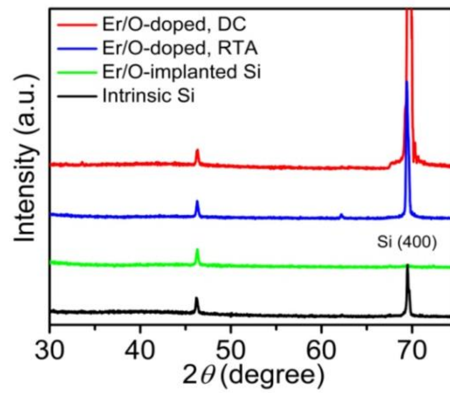

Figure S16. XRD characterization. XRD patterns of DC- (red line) and RTA-processed (blue line) Er/O-Si samples. As comparison, XRD results of Er/O-implanted (green line) and intrinsic (black line) silicon samples were also included in this figure.

Supplementary References

[R1] W. Kohn, L. J. Sham, *Phys. Rev.* **1965**, 140, A1133.

[R2] H. J. Monkhorst, J. D. Pack, *Phys. Rev. B* **1976**, 13, 5188.

[R3] L. Liu, L. Yao, K. Feng, Z. Luo, K. Liu, Hong Zhu, P. K. Chu, *Coatings*, **2018**, 8, 386.